Numerical Investigation on Aerodynamic Performance of Bird's Airfoils

Ashraf Omar[1,2,*], Rania Rahuma[2], Abdulhaq Emhemmed[2]

Omar A https://orcid.org/0000-0003-3321-0728
Rahuma R https://orcid.org/0000-0002-9269-8332
Emhemmed A https://orcid.org/0000-0002-9090-8404

How to cite

ABSTRACT: In this work, the aerodynamic performance of four types of bird's airfoils (eagle, stork, hawk, and albatross) at low Reynolds number and a range of angles of attack during fixed (unflapping) gliding flight was numerically investigated utilizing open-source computational fluid dynamics (CFD) code Stanford University unstructured (SU2) and K-ω Shear Stress Transport (K-ω SST) turbulence model. The flow of the simulated cases was assumed to be incompressible, viscous, and steady. For verification and comparison, a low Reynolds number man-made Eppler 193's airfoil was simulated. The results revealed that stork has the greatest aerodynamic efficiency followed by albatross and eagle. However, at zero angle of attack, the albatross aerodynamic efficiency exceeded all the other birds by a significant amount. In terms of aerodynamics efficiency, stork's and albatross's airfoils performed better than Eppler 193 at angles of attack less than 8°, while at a higher angle of attack all studied birds' airfoils performed better than Eppler 193. The effect of surface permeability was also investigated for the eagle's airfoil where the permeable surface occupied one-third of the total airfoil surface. Permeability increased the generated lift and the aerodynamic efficiency of the eagle's airfoil for angles of attack less than 10°. The increase reached 58% for the lift at zero angle of attack. After the specified angle, the permeability had an adverse effect on the flow which may be due to the transition to turbulent ahead of the permeable section.

KEYWORDS: Bird's airfoils; SU2 CFD suite cod; Low Reynolds number flow; Birds' aerodynamics; Airfoil's permeability.

INTRODUCTION

In general, everything in life is inspired by nature. Birds are a wonder of nature; their flapping and unflapping flight reaches a level of perfection in all ways. Many birds use nonflapping flight mode to modulate their power during intermittent flight (Tobalske 2007). The fundamentals of bird flight are similar to those of an aircraft (Ali *et al*. 2017). In the area of low Reynolds number flow, such as for microaerial vehicles (MAVs) and unmanned aerial vehicles (UAVs), birds' wings have excellent performances over man-made MAVs wings (Jacob 1998; Lees 2016; Yang and Song 2017). In other words, low Reynolds aerodynamics are important for both natural and man-made flying vehicles, especially in the area of small aircraft development, such as UAVs and MAVs. Therefore, lessons can be learned from bird features and flight performance.

The bird's wing base generates different aerodynamic forces than the tip due to its noncambered and thinner outer half of the wing in comparison with the cambered and thicker wing's inner half (Thielicke 2014). Birds need high force coefficients at slow flight speeds. For birds, there are two kinds of moving wings operating in two different modes: nonflapping mode (gliding) and flapping mode (oscillating). As explained by Shyy *et al*. (2007), nonflapping birds stretched out their wings to produce lift and the generated thrust can be produced by gravity force during the descending flight (gliding). Many gliding birds, such as stork and

albatross, appear to hang effortlessly in the air and gain height by barely twitching their wings. This is due to their high lift to drag ratio (aerodynamic efficiency), which is resulted from their wings generating a lot of lift without producing much drag. Big birds have evolved to be gliders partly due to their big wings. Also, birds and insects can generate relatively large force very quickly in response to gusts and other disturbances during perching manoeuvres (Dvořák 2016). However, more detailed investigations are needed in this field to improve the general understanding of the bird's flight feature mechanisms.

Carruthers *et al.* (2010) analysed the drag of an eagle's airfoil over Reynolds number in the range of 10^5 to 2×10^5. They concluded that the drag is almost constant over a wide range of lift coefficient. Withers (1981), however, observed that the pattern of the flow over the bird wing is consistent with the aerodynamics theory for man-made low Reynolds number airfoils and has poor aerodynamic performance in comparison to high Reynolds number airfoils. The lift coefficient of dried and replica pigeon wings was estimated by Usherwood (2009) using a direct measurement of forces and mapped forces of pressure distribution. The lift coefficient of 1.64 was measured for dried surface and 1.44 for the replica surface.

Normally, the birds use the gliding flight mode to save energy (Videler and Groemewold 1991). A trained pigeon was used in a wind tunnel by Tucker and Parrott (1970) to investigate its gliding performance in a more accurate sense. They concluded that the falcon achieved the maximum possible lift-to-drag ratio (L/D) over its range of gliding speeds by adjusting its wingspan. Tucker and Heine (1990) conducted wind tunnel testing to study the gliding aerodynamic characteristics of a Harris' hawk. The maximum lift coefficient was measured as 1.6 and the minimum profile drag coefficient was found to be 0.026 at a lift coefficient of 0.6. No-stall condition was observed for the wing during the testing which made them believe that the actual maximum lift was lower than the measured one. The study of the dynamics of the soaring albatross by Sachs *et al.* (2013) shows that the primary energy gain from the shear wind reaches the necessary energy for sustained nonflapping flight. Tang *et al.* (2019) extracted golden eagle's airfoil configuration from its wing using a 3D laser scanner to establish a traditional airfoil. Their study indicates that the existence of the secondary feather does not change the steady aerodynamic coefficients, but the lift and drag were enlarged by 71.9 and 206.1%, respectively due to the large chord length.

There are many researchers inspired by the aerodynamic of birds, flyers, and swimmers in designing their airfoils and wings to improve the aerodynamics performance of man-made flying vehicles. There are several bird-like airfoils built and tested by researchers (Ge *et al.* 2013; Kozlov *et al.* 2015; Fish *et al.* 2016; Mandadzhiev *et al.* 2016; 2017; Flint *et al.* 2017; Sheppard and Rival 2018; Malik *et al.* 2019). For example, bird-like airfoils serial AS6091 to AS6099 were designed by Ananda and Selig (2018) to meet MAVs requirement of efficient flight at low Reynolds number. All designed airfoils were characterized by a bulbous leading edge followed by a thin feather-like after region. All designed airfoils showed good aerodynamic performance.

A review of the aerodynamics of nonflapping bird wings was carried out by Aldheeb *et al.* (2016). They presented an overview of prior analyses and experiments on the aerodynamic performance and mechanical properties of birds in steady nonflapping flight. They concluded that there are some areas of high complexity in bird aerodynamics that need more study such as wing flexibility and porous surfaces.

Porosity of the wing is a feature of importance in the bird's aerodynamics. Studying this effect, Iosilevskii (2011) divided the wing membranes into solid and porous segments. Bird wing porosity leads to a significant difference in the air transitivity between inner and outer feather vanes. The understanding of the air flow when it penetrates through feathers was the focus of many studies in the field of bird aerodynamics (Müller and Patone 1998; Geyer *et al.* 2010; Iosilevskii 2013; Béguin and Breitsamter 2014; Yu 2014). Aerodynamic forces due to porosity and their effects on the wing flexibility were examined by Béguin and Breitsamter (2014). It was found that the aerodynamic forces can deform the wing surface based on the aerodynamic conditions. Air transitivity of feathers from the ventral to the dorsal direction and vice versa was studied by Müller and Patone (1998). They concluded that both directions have a small difference in air transitivity that is about 10%. However, a significant difference occurs in air transitivity between inner and outer feather vanes. Iosilevskii's (2013) analytical study showed that by keeping the width of the porous segment to less than half of the wing's chord, the drag can be contained. The continuously distributed porous surface on the airfoil was used by Eppler (1999) to control the flow separation by applying suction pressure under the porous surface. As observed by some researchers in this field (Zhao and Zhao 2014; Jiao and Lu 2015; Chapin and Benard 2015), the location and the angle of the controller segment were the most important parameter in delaying flow separation. Comprehensive

experimental works were carried out by Aldheeb *et al.* (2018) to investigate the aerodynamics of the symmetrical thin porous rectangular half wing and its airfoil section. They concluded that the lift slope decreased as the porosity increased and the drag decreased at a low value of porosity and then increased as porosity increased. In other research work by Aldheeb *et al.* (2020), they investigated experimentally, using particle image velocimetry (PIV), the effect of the porous wingtips with directional porosity on the flow field over the wingtip surface and its impact on the vorticity. They concluded that the directional porosity during the landing can be used as wake vortex alleviation.

The presented bibliographic survey shows that the focus of the most research work in this field was on the design of bird-like airfoils or the aerodynamics characterises of the birds' airfoils. There is a need for a comparison study to relate the aerodynamics characterises for each bird's airfoil with their flight behaviour.

The main goal of this work is to numerically study the aerodynamic performance of four different bird's airfoils at low Reynolds number during fixed (nonflapping) gliding flight mode. The four selected birds were eagle, stork, hawk, and albatross. The selected birds that have different flight behaviours were stork and albatross, that are migratory birds, but fly at different altitudes. The albatross flies near the water surface at very low altitude. The eagle and hawk are predators, where the former attacks prey from high altitudes at very fast speeds and the latter uses a different feeding strategy involving catching flying insects in the air. The study also examines the effect of porosity on the aerodynamics characterises of the airfoil.

The study was carried out using open source CFD suite Stanford University unstructured (SU2) code developed by teams from different universities lead by Aerospace Design Laboratory (ADL) from Stanford University (Economon *et al.* 2016). The aerodynamics performance of the selected bird's airfoils was compared with man-made low Reynolds airfoil Eppler 193 (Selig *et al.* 1989).

MATERIAL AND METHODS

AIRFOIL GEOMETRY AND MESH GENERATION

The four selected bird's airfoils for this study were eagle, stork, hawk, and albatross. The actual shapes of the selected airfoils, shown in Fig. 1, were found in White (2008). The selected airfoils were scaled and drawn using XFLR (XFLR5 2016). The man-made low Reynolds number airfoil Eppler 193 (Selig *et al.* 1989; UIUC 2020) was used in this study for CFD mesh setup, verification, and comparison.
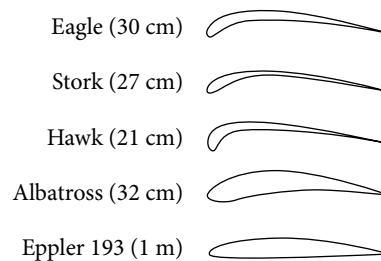

Figure 1. Shape and chord length for the airfoils.

The eagle's, stork's, and hawk's airfoils are categorized in the same family, they have an average maximum camber to chord ratio of 9% located between 27 and 30% of the chord, while the maximum thickness to chord ratio occurs at around 6% and has a value between 7 to 10% of the chord. However, the albatross is an exception, because it has a similar maximum camber, but it is located at around 40% of the chord. The maximum thickness to chord ratio is greater and is equal to 12% located at approximately 20% of the chord. The coordinates for the E193 airfoil were found in many sources such as Selig *et al.* (1989) and UIUC (2020) (Fig. 1).

The airfoil geometries were then imported into a mesh generation software. As experimental results are available for the Eppler 193 airfoil, it was meshed and simulated first. This allowed the verification before the simulation of the bird's airfoils. It also provided intuition about the required mesh size and its effects on the results. The mesh was a structured C-H mesh type with quad cells. Following the recommendation by the NASA turbulence modelling group (NASA 2017; 2019; 2020), the computational domain of the far boundary was set to be around 300 chord lengths behind the airfoil and 100 above, below, and in front of the airfoil. This had been done to eliminate any effects of backflow. In addition, the first mesh layer was placed at a distance of 10^{-6} m from the airfoil surface. This was made to obtain a y+ less than 1. The air temperature of 287.5 K, the average velocity of 13.5 m/s, the density of 1.21328 kg/m³ and dynamics viscosity of 1.80881×10^{-5} N s/m² were used to calculate the required first layer thickness for each airfoil as presented in Table 1. The mesh size was approximately 122,000 cells for nonpermeable airfoil and 155,000 for the permeable airfoil. Figure 2 shows the mesh for the eagle's airfoil at different views.

Table 1. Reynolds number and required minimum wall spacing for the airfoils.

Airfoil	Reynolds Number	Required Minimum Wall Spacing (m) for Y+= 1
Eagle	271658	2.26646E-05
Stork	244492	2.24270E-05
Albatross	208271	2.20703E-05
Hawk	190160	2.18704E-05
E193	100000	2.05090E-05

(a)

(b)

(c)

All domain.

Mesh near trailing edge.

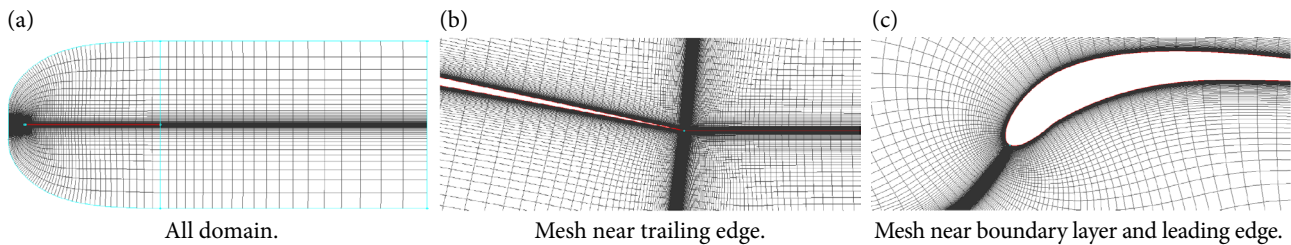Mesh near boundary layer and leading edge.

Figure 2. Mesh around eagle's airfoil.

The quality of the mesh was measured by the cell skewness value. The cell skewness method is one of the primary methods used to check the quality of the mesh. The best skewness for a quad cell is 0, meaning all sides make right angles. Having a mesh with a large number of cells that are highly skewed (≥ 0.8) will cause instability and inaccuracy in the numerical solution (Mesh Quality 2009). The most cells of the generated mesh have a skewness of 0 while only a few cells are modularly skewed.

NUMERICAL SIMULATION

As mentioned in the Introduction, all the cases in this work were simulated using SU2 CFD code (Economon *et al.* 2016). The code has solvers for several models including Reynolds averaged Navier–Stokes (RANS), wave equation, heat equations, and equations that model solid mechanics. For RANS, SU2 provides a solver for both incompressible and compressible flow.

The boundary conditions used were far-field boundary conditions (free stream) for the edge of the computational domain. For the airfoil surface, the no-slip boundary condition was used. The solved equations of motion that modelled the fluid flow were RANS equations. All the simulations were run using a Courant-Friedrichs-Lewy (CFL) number of 10. Approximately 40,000 iterations were run before the code converged for all cases.

The bird's airfoil was assumed to be in steady gliding mode while the flow was assumed to be 2D incompressible. Average velocity for general birds was approximated as 13.5 m/s (Aldheeb *et al.* 2016) and gliding attitude was set to 100 m. All studied airfoils were run in simulations for angles of attack ranging from 0 to 20°. The main differences between the simulations were the Reynolds number (*Re*), because each bird flies/glides at a certain speed and they all have different chord length. However, for all cases, *Re* is regarded as falling in the range of 10^5 to 2.7×10^5.

VERIFICATION

The CFD solver was verified against experimental measurements for the E193 airfoil obtained by Selig *et al.* (1989). The verification case was tested for mesh size, boundary conditions and turbulence model type (Spalart–Allmaras, SA and K-Omega shear stress transport, k-ω SST models).

Figure 3 shows the variation of the lift and drag coefficients at different angles of attack for the E193 airfoil. It compares the experimental and simulation results obtained using SA and K-*ω* SST models. The comparison for the maximum lift coefficient is summarized in Table 2. It can clearly be seen that at a low angle of attack (α), the results obtained from both models agree well with the experimental results. However, as the angle of attack increases, a divergence between the simulation and the experimental results is observed. This divergence is greater for the SA model, which suggests that the K-*ω* SST model is better suited to this application.
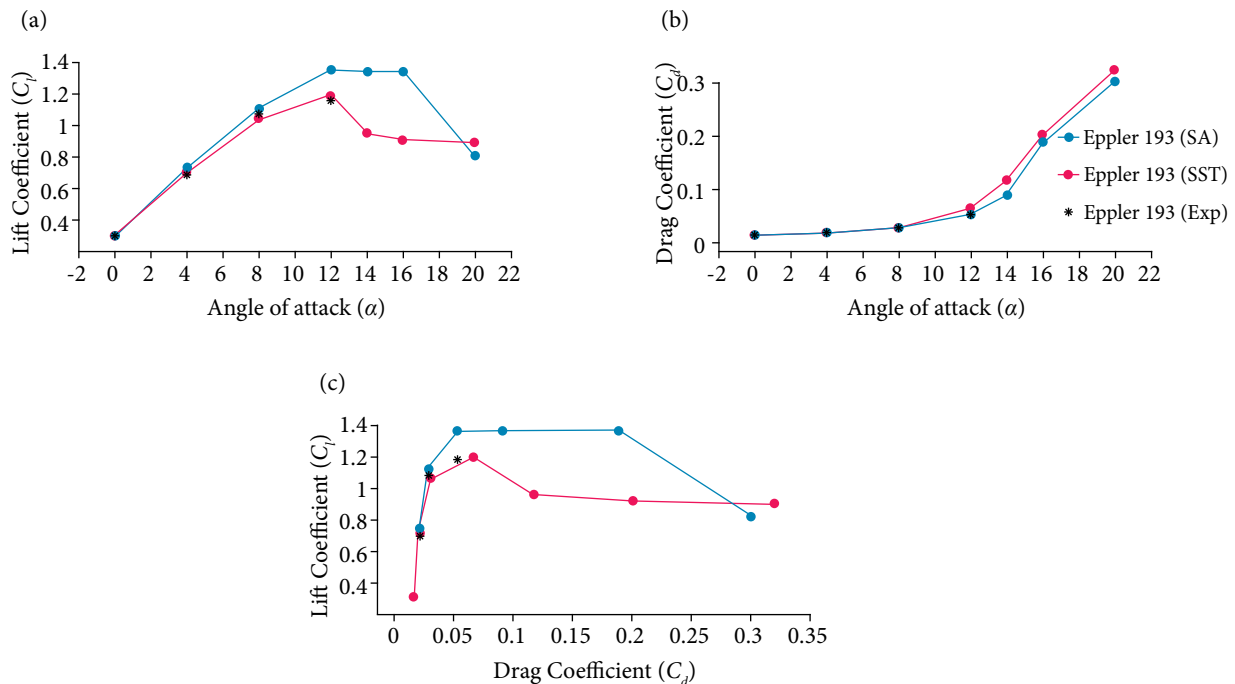
(a)

(b)

(c)

Figure 3. Validation of lift and drag coefficient.

Table 2. C_{lmax} at α_{stall} for E193 airfoil.

Airfoil	α_{Stall}	C_{lmax}	Error (%)
E193 (Experimental)	12°	1.16	-
E193 (SST)	12°	1.18	1.72
E193 (SA)	12°	1.35	16.37

RESULTS AND DISCUSSION

The numerical simulation was carried out for the four selected bird's airfoils (eagle, stork, hawk, and albatross) and man-made low Reynolds airfoil Eppler 193 at angles of attack ranging from 0 to 20°. The numerical results were presented in terms of lift and drag coefficients, pressure distribution, streamlines, and aerodynamics efficiency. The effect of the airfoil permeability was also studied for the eagle's airfoil where the aerodynamics of the nonpermeable airfoil were compared to those of the permeable airfoil.

NONPERMEABLE AIRFOIL

Lift coefficients versus angle of attack for the studied airfoils are shown in Fig. 4. When comparing the birds' aerodynamic performance, it can be noticed that at a zero angle of attack, eagle, stork, and albatross have the highest lift coefficient (C_l). In addition, for overall angles of attack, stork and eagle have the highest C_l and nearly the same behaviour. Although the albatross has a value of C_l higher than the hawk at an angle of attack (α) less than 8°, the behaviour changes thereafter and the hawk generates larger lift. It has been noted that the E193 airfoil has the lowest C_l. In terms of the lift coefficient slope, Fig. 4 clearly shows that the hawk has the highest slope, followed by eagle and stork, then E193, with the albatross having the lowest slope but the highest stalling angle of attack in comparison with the rest. This observation indicates the hawk's ability to gain fast lift in comparison with the other bird's airfoils, while the albatross's airfoil was able to maintain a high lift coefficient as the angle of attack reached a higher value. The maximum lift coefficient at stalling angles of attack for all airfoils is summarized in Table 3. Inspecting the behaviour for all airfoils beyond the stalling angle of attack (α_{stall}) shows a dramatic decrease in C_l except for the albatross's airfoil where a slight lift recovery was observed after exceeding the stall angle of attack, this could be due to the increase of the positive pressure area.
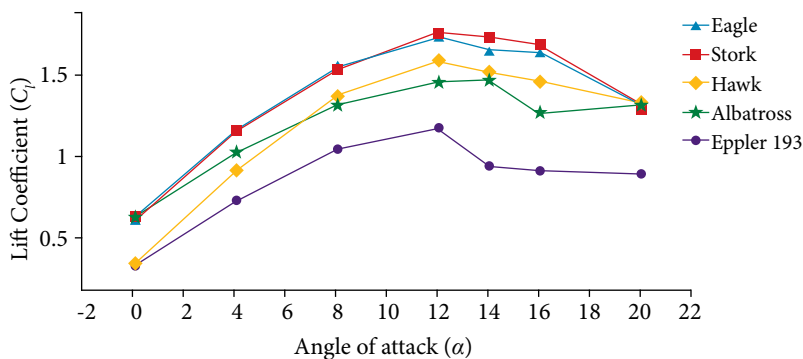

Figure 4. C_l vs α for studied airfoils.

Table 3. Airfoils C_{lmax} at α_{stall}.

Airfoil	α_{stall}	C_{lmax}
Eagle	12°	1.74
Stork	12°	1.77
Albatross	14°	1.49
Hawk	12°	1.61
E193	12°	1.18

Figures 5 and 6 show the drag polar and the variation of the drag coefficient (C_d) with respect to α. The behaviour of a slowly increasing of C_d and a sharply increasing of C_d after reaching $(C_l)_{max}$ was seen. It can be noted from Fig. 5 that the albatross's airfoil gives maximum lift coefficient versus drag coefficient at zero angle of attack while the stork's airfoil gives maximum lift coefficient versus drag coefficient at a high angle of attack. In terms of drag coefficient vs angle of attack, Fig. 6 shows that the hawk's airfoil has the highest C_d while the E193 airfoil has the lowest C_d for angles of attack below 10° and for higher angles of attack, the lowest C_d was observed for the albatross and highest for the Eppler 193. As shown in Fig. 6, the trend of rate of increasing C_d with respect to the angle of attack is similar for all studied airfoils until the stall angle of attack but as the angle of attack exceeds the stall, the drag coefficient trend behaves differently where the highest rate was observed for the Eppler 193 and the lowest rate for the albatross.
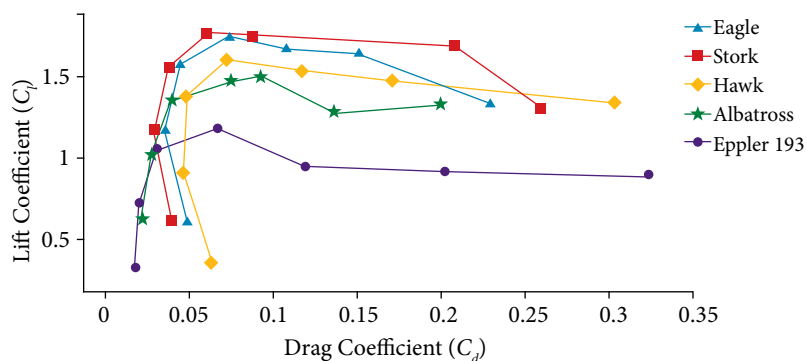
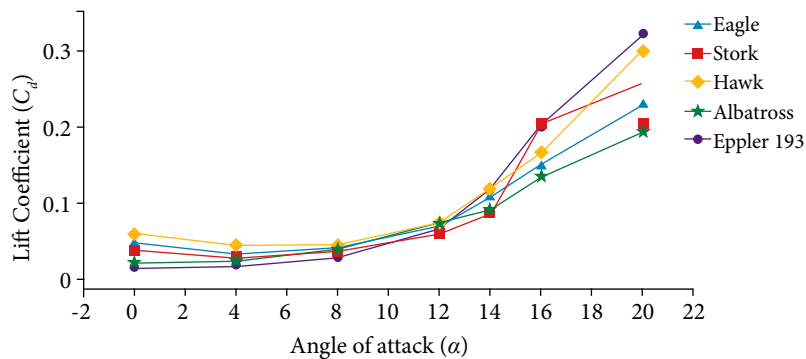**Figure 5.** Drag polar curves of the studied airfoils.

Figure 6. Variation of the drag coefficient vs angle of attack of the studied airfoils.

To have a better understanding of the aerodynamic performance of the studied airfoils, the lift to drag ratio was compared, as shown in Fig. 7. It can be clearly seen in Fig. 7 that the stork has the best overall aerodynamic efficiency at high angles of attack, but the albatross has the best aerodynamic efficiency at zero angle of attack, while the hawk has the lowest overall aerodynamic efficiency. The result is consistent with the nature of these birds (gliding at low altitudes) and this observation agreed with Shyy *et al.* (2007) and Bonnin (2016).

Table 4 shows that the best aerodynamic efficiency occurs at an angle of attack equal to 8° for the eagle and the hawk and 4° for the albatross and the Eppler 193. However, for the stork's airfoil, the aerodynamic efficiency curve in Fig. 7 is smooth and almost flat at an angle of attack ranging between 4 and 8° where the maximum aerodynamic efficiency occurred. This flat region of the curve has the advantage of controlling the adverse pressure gradient to prevent flow separation.
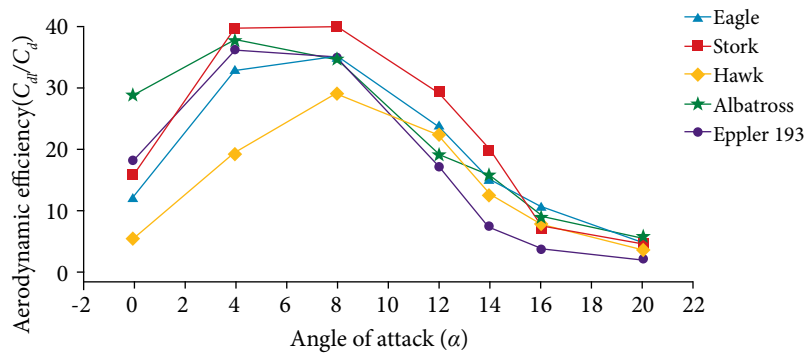
Figure 7. Aerodynamics efficiency of the studied airfoils.

Table 4. $(C_l/C_d)max$ for the studied airfoils.

Airfoil	Angle of Attack (α)	$(C_l/C_d)max$
Eagle	8°	35.46
Stork	4°-8°	40-40.19
Hawk	8°	29.19
Albatross	4°	37.93
E193	4°	36.18

As the variation of C_l and C_d, the distribution of the pressure coefficient (Cp) shown in Fig. 8 follows a general pattern. At the stagnation point, the coefficient is equal to 1; therefore, a value of one will be observed at a certain point on the airfoil surface. This usually occurs on the upper surface. Furthermore, the distribution on the upper surface after these points tends to decrease until it reaches a minimum value $(Cp)min$ which is called a suction peak. Afterwards, the pressure increases gradually until the trailing edge. This region is called the adverse pressure gradient region as in this region flow separation may occur especially if the pressure increase rate was severe. The lower surface exhibits similar behaviour although the change is very gradual which makes the upper surface more important when considering flow control. An important property related to the suction peak is when it occurs, for some airfoils it occurs very late (further downstream) which is favourable to avoid separation and the opposite for other airfoils. It can be clearly seen from the Fig. 8 that the albatross has the furthest suction peak point where it occurs at approximately 30% of the chord. It decreases as the angle of attack increases. Similarly, the other airfoils have their peak suction pressure at a range of 5 to 20% of the chord at zero angle of attack, decreasing thereafter. It was observed that the hawk and the eagle have the lowest suction pressure for the angles of attack of 0 and 4°. At angles of attack of 8, 12 and 14°, the E193 has the lowest suction pressure; however, it increases when the angle of attack is equal to or higher than 16°.

The streamlines around each bird airfoil are shown for different angles of attack in Fig. 9. It can be seen in Fig. 9a where α = 0° that the circulation occurs on all airfoils except on the albatross's airfoil. The circulation is greatest for the hawk's airfoil. This can be related to the aerodynamic performance at zero angle of attack as discussed earlier where the albatross had the highest efficiency while the hawk had the lowest. A possible explanation is that the thickness of the albatross airfoil allows for smoother flow while all the other airfoils are thin and have a large camber near the leading edge. This suggests that the intensity of the circulation can be greatly influenced by the airfoil camber and thickness. As α reaches the stall angle (Fig. 9b), it has been noticed that the stork's airfoil is more efficient compared to the other birds' airfoils where no separation was observed. This explains why the stork's airfoil has the highest lift coefficient (1.77) as shown in Table 3. As shown in Fig. 9b, there is a similarity in flow streamlines pattern for the hawk and eagle, but Table 3 shows that the eagle has a higher maximum C_l. This could be due to the location of the separation and the size of the separation bubble. The large separation area and bubble in Fig. 9b for the albatross explains why the albatross has the lowest maximum C_l among the studied airfoils as shown in Table 3. Finally, for a large angle of attack (α = 16°) as shown

in Fig. 9c, the flow separation exists for all bird's airfoils. This causes loss in the lift and hence reduction in aerodynamic efficiency. At this high angle of attack, lift and drag coefficient from Figs. 4 and 6 can be related to the streamlines in Fig. 9c where the separation location and size of the bubble highly affect the value of the lift and drag coefficient where the stork has the highest lift and drag coefficient and the albatross has the lowest.
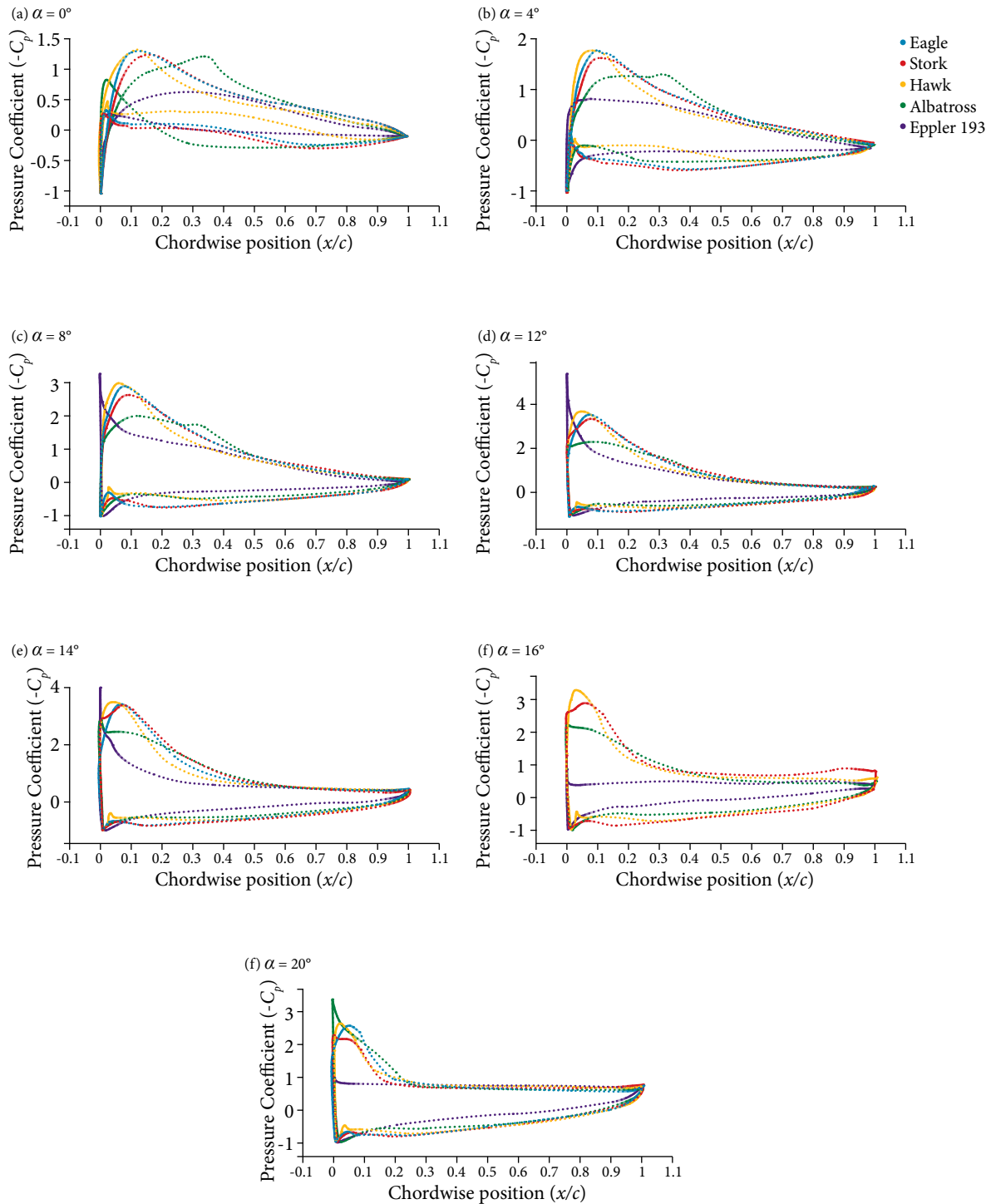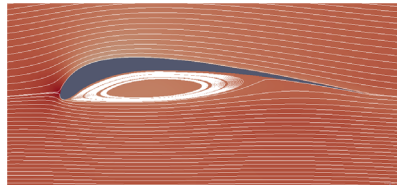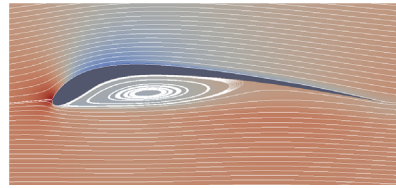

Figure 8. Pressure coefficient distribution for studied airfoils at various angles of attack.
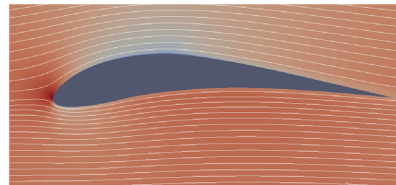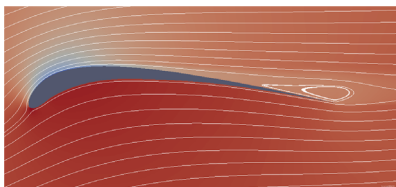
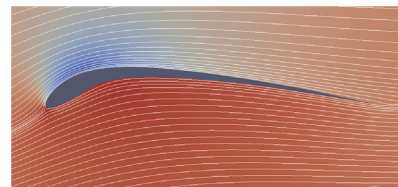(a) $\alpha = 0°$

Eagle's airfoil
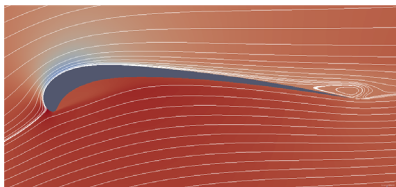
Stork's airfoil
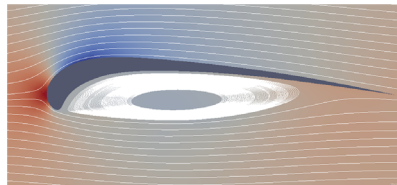
Hawk's airfoil

Albatross's airfoil

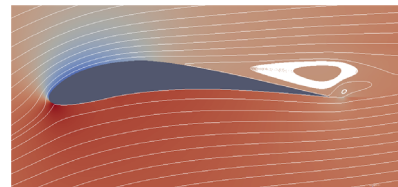(b) $\alpha = 12°$ for eagle's, stork's and hawk's airfoils; 14° for albatross's airfoil
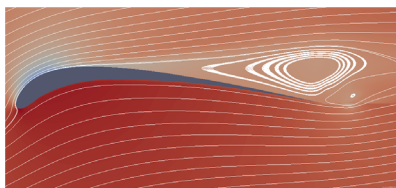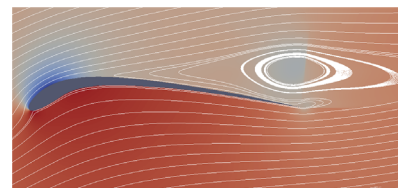
Eagle's airfoil

Stork's airfoil

Hawk's airfoil
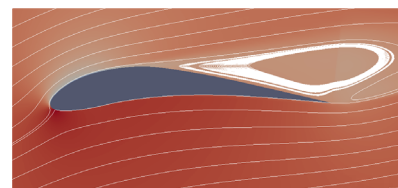
Albatross's airfoil

(c) $\alpha = 16°$

Eagle's airfoil

Stork's airfoil

Hawk's airfoil

Albatross's airfoil

Figure 9. Exhibition of streamlines at different angles of attack for all four bird's airfoils.

All the discussed results can be related to the nature of each bird's flight, even though the study was done only for 2D cases. For example, the stork flies at high altitude and for long ranges during migration (Pennycuic 1972). This explains its high aerodynamic efficiency at high angles of attack. The albatross is also a migratory bird; however, it usually uses unflapping flight mode to travel large distances at low altitude near the water surface (Sachs *et al.* 2013). This may explain why the albatross has best performance at zero angle of attack. Finally, the eagle is a predator that attacks prey from high altitudes at very fast speeds (Pennycuic 1972). To do so, it requires high aerodynamics.

PERMEABLE AIRFOIL

Naturally, the eagle has been chosen to investigate the phenomena concerned with permeability nature due to its existence within the global environment; in addition, this kind of bird has been trained by humans to help them in hunting. Furthermore, the bird configuration is acceptable due to its unique flight behaviour. All of the above characteristics made it interesting to observe the effect of permeability for the eagle's airfoil.

The presented data for the nonpermeable eagle's airfoil is the same as the one discussed in the previous section; it has been repeated here to allow comparison with the permeable airfoil. The porosity was modelled by considering one-third of the airfoil chord toward the trailing edge to be a flat plate with holes at every 0.25 cm spacing as shown in Fig. 10. The SU2 code allowed the definition of permeable cells and application of symmetry wall boundary conditions to them. This will allow the flow to pass through the lower surface holes to the upper surface with the same flow properties. In other words, the pressure and velocities of the lower and upper surfaces are maintained the same and their values are updated for each iteration. The no-slip condition was used for the airfoil solid surface.
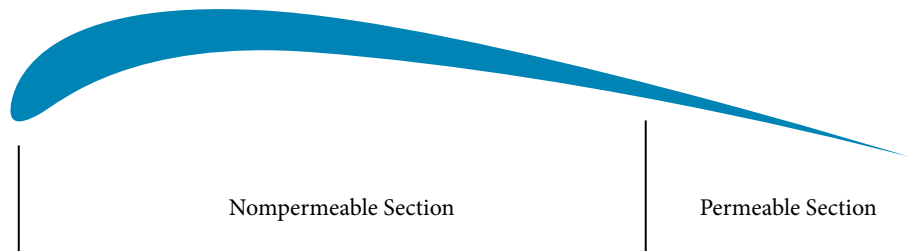
Nonpermeable Section   Permeable Section

Figure 10. Eagle's airfoil with permeable section.

Figure 11 shows the variation of C_l, C_d, and C_l/C_d for the permeable and nonpermeable eagle's airfoil. Table 5 shows the maximum C_l at the stalling angle of attack for the nonpermeable and permeable airfoil. Although the permeable airfoil stalls earlier, it is clear from Fig. 11 that it generates higher lift in comparison to the nonpermeable at an angle of attack lower than the stall angle. The increase reached 58% at a zero angle of attack. In term of the minimum drag coefficient, the permeable airfoil performs better than nonpermeable airfoil for the angle of attack less than 12° but this trend is reversed for a higher angle of attack. The variation of the aerodynamic efficiency parameter C_l/C_d can be also seen in Fig. 11. The aerodynamic efficiency parameter clearly shows the positive effect of the permeability for low angles of attack. Having a permeable section on the airfoil surface will provide better aerodynamic characteristics when the angle of attack is less than 10°. This is compatible and in agreement with the observation of other researchers on the effect of the holes on the aerodynamics characteristics of the airfoil that concluded that "at a transitional phase where *Re* = 40,000 and the angle of attack ranged from 0 to 9°, the L/D ratio was higher compared to the same wing without holes" (Aldheeb *et al.* 2016). It seems that at an angle of attack greater than 10°, the flow becomes turbulent or separated before reaching the permeable part of the airfoil. In this situation, the existence of the permeable part worsens the conditions causing less lift to be generated. This can be clearly seen in the pressure distribution curves in Fig. 12. This conclusion agreed with the observation of Zhao and Zhao Q. (2014), Jiao and Lu (2015) and Chapin and Benard (2015) on the importance of the control segment

location in delaying the flow separation. It can be concluded that the maximum lift coefficient of the eagle's airfoil can be reached at a lower angle of attack by applying the permeability to the one-third of the airfoil chord, though, after the specified angle, the permeability had adverse effects on the flow that could be due to the transition to turbulent ahead of the permeable section.

Table 5. C_{lmax} at $\alpha stall$ for a permeable and nonpermeable eagle's airfoil.

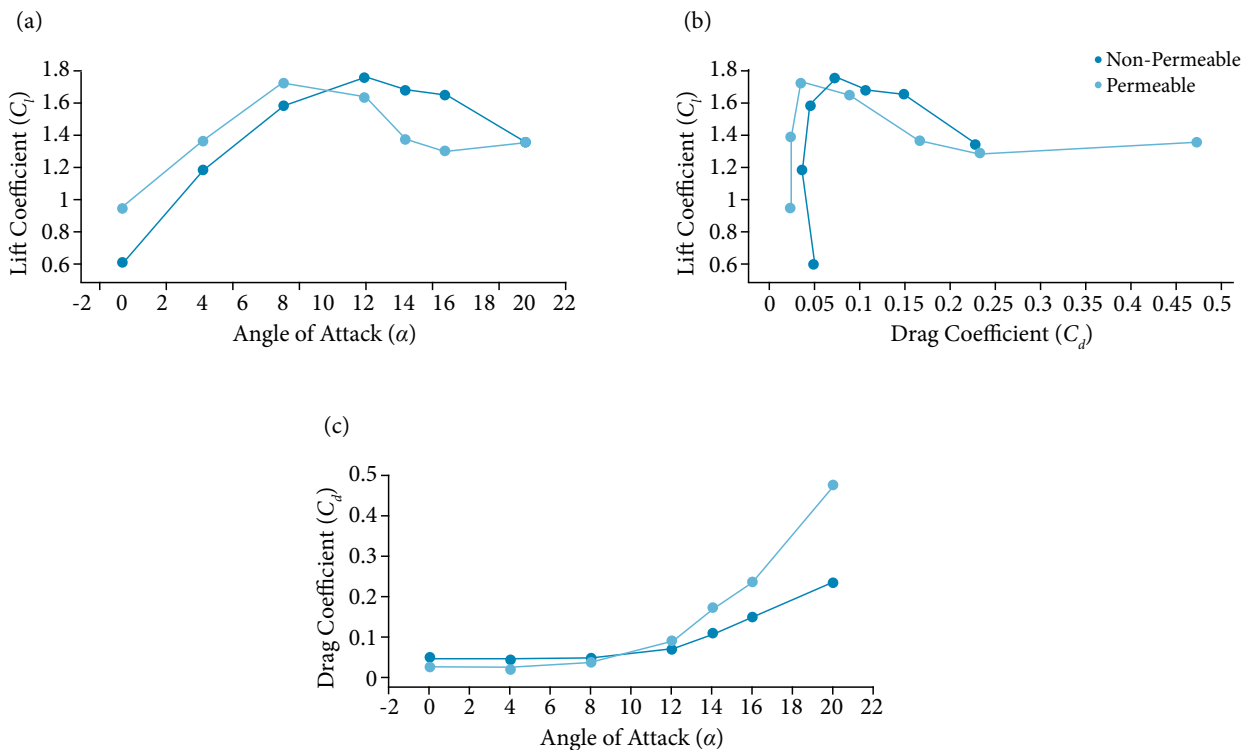| Airfoil	αstall	C_{lmax}
Nonpermeable airfoil	12°	1.74
Permeable airfoil	8°	1.71

(a)

(b)

(c)

Figure 11. Variation of lift coefficient, drag coefficient and lift to drag ratio for nonpermeable and permeable airfoils.

The advantages of the permeable airfoil at the stall angle of attack is demonstrated by pressure distribution curves and streamlines, as shown in Figs. 12 and 13. Figure 12 shows that the maximum suctions pressure is higher for the permeable airfoil until $\alpha > 14$ where it becomes lower. This suggests that permeability affects the flow upstream making the flow reach higher velocities compared to the nonpermeable airfoil. The location of the maximum suction pressure and the pressure gradients on the airfoil surfaces can be also observed in Fig. 12. The location is almost the same for both cases. Furthermore, the adverse pressure gradient for the permeable airfoil is severe at high angles of attack. In Fig. 13, the streamline pattern shows that the separation has taken place at its trailing edge for nonpermeable airfoil, but, for the permeable airfoil, no separation was observed, and the streamlines are smooth. As shown in Fig. 14, as the angle of attack increases beyond the stall angle of attack, flow separation appears to exist for both airfoils. However, the permeable eagle's airfoil has more severe separation than the nonpermeable eagle's airfoil. This explains the loss of the lift for the permeable airfoil at higher angles of attack.

(a) $\alpha = 0°$

(b) $\alpha = 4°$

• Non-Permeable
• Permeable

(c) $\alpha = 8°$

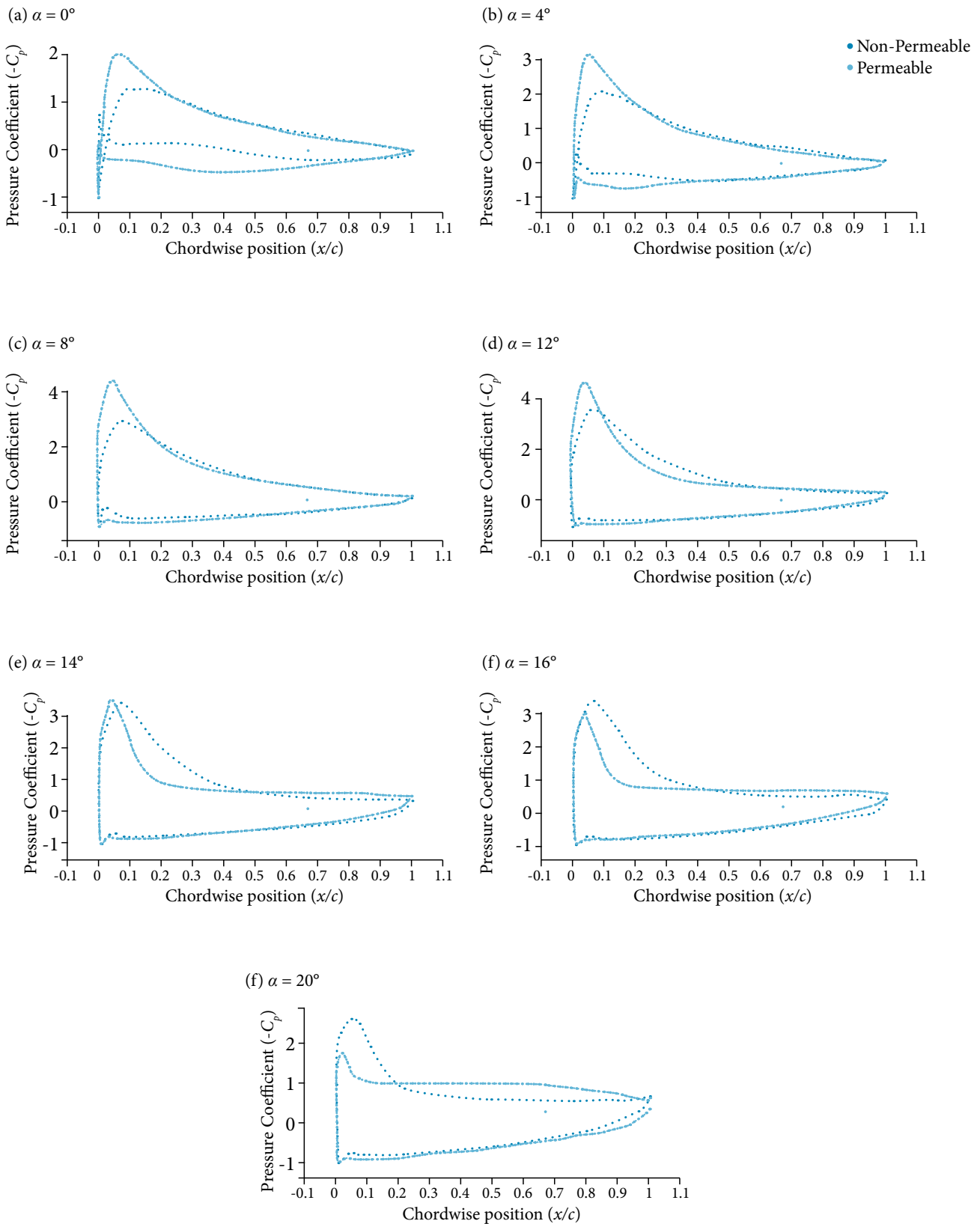(d) $\alpha = 12°$

(e) $\alpha = 14°$

(f) $\alpha = 16°$

(f) $\alpha = 20°$

Figure 12. Pressure coefficient distribution for a permeable and nonpermeable airfoil at various angles of attack.

(a)

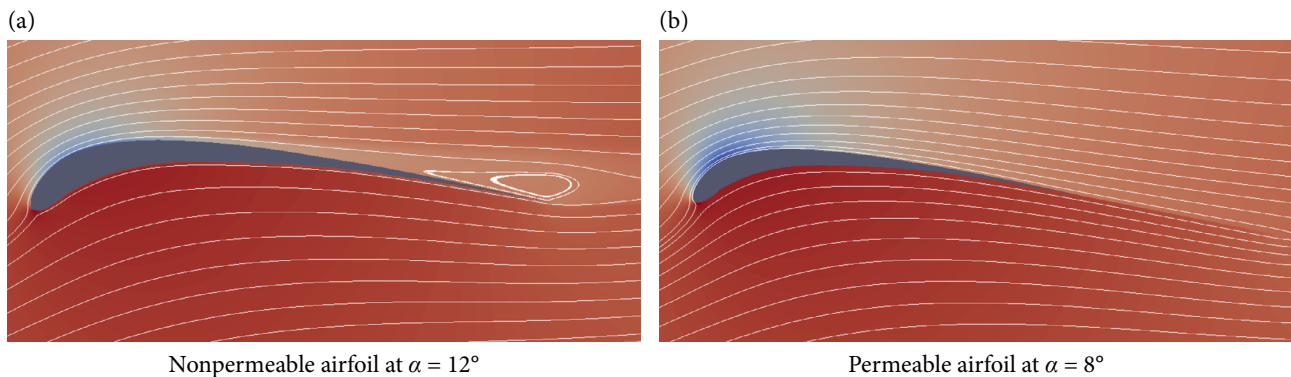Nonpermeable airfoil at $\alpha = 12°$

(b)

Permeable airfoil at $\alpha = 8°$

Figure 13. Exhibition of streamlines at stall angle of attack for permeable and

(a)

Nonpermeable airfoil at $\alpha = 16°$

(b)

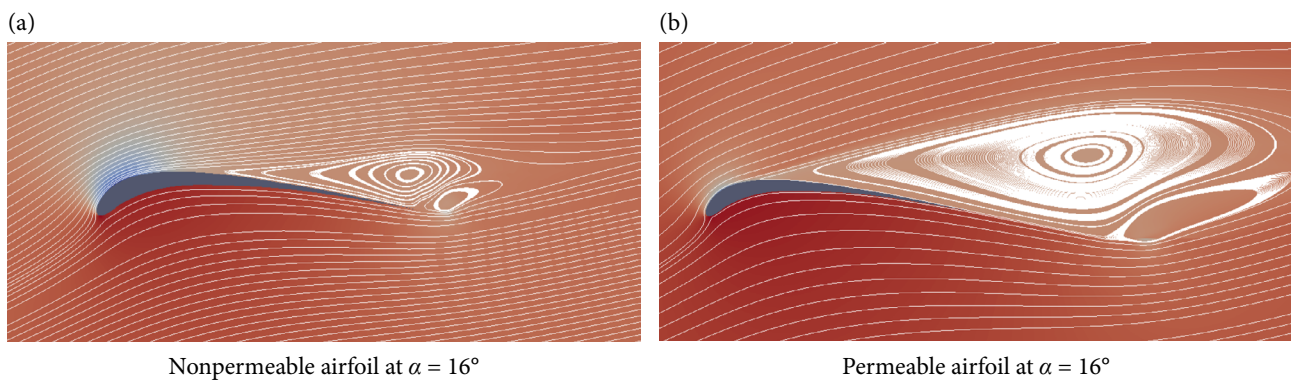Permeable airfoil at $\alpha = 16°$

Figure 14. Exhibition of streamlines at high angle of attack for permeable and nonpermeable eagle's airfoils.

CONCLUSION

This paper has presented the aerodynamic performance of four different bird's airfoils: eagle, stork, hawk, and albatross. The bird's airfoils were compared to a man-made low Reynolds airfoil Eppler 193. The study was carried out numerically using the SU2 open-source CFD code. A reasonable agreement has been achieved between the obtained simulation results using a K-ω SST turbulence model and the experimental data for the Eppler 193 airfoil case.

In terms of aerodynamic efficiency, at a low angle of attack (less than 8°) the Eppler 193 performs better than the eagle and the hawk but shows poorer performance than the stork's and albatross's airfoils. At an angle of attack of 8°, the Eppler 193 aerodynamically performs the same as the eagle and the albatross, lower than the stork and higher than the hawk. For an angle of attack of 10° and higher, the results revealed that the eagle, stork and albatross's airfoils perform aerodynamically better than the Eppler 193 airfoil. The highest aerodynamic efficiency at zero angle of attack was observed for the albatross while the stork has the highest aerodynamic efficiency for an angle of attack ranging from 4° to 8°. Among the four selected bird's airfoils, the hawk has the poorest aerodynamic efficiency at an angle of attack below 10°.

The study also investigated the effect of the surface permeability on the aerodynamic performance of an eagle's airfoil. It was found that introducing the permeability to the eagle's airfoil surface improves the aerodynamic efficiency for an angle of attack below 10°, nonetheless, it had adverse effects for higher angles of attack.

AUTHOR'S CONTRIBUTION

Conceptualization: Omar A; Methodology: Rahuma R; Computational Works: Rahuma R and Emhemmed A; Analysis: Omar A; Rahuma R and Emhemmed A; Writing – Original Draft: Rahuma R and Emhemmed A; Writing – Review and Editing: Omar A; Supervision: Omar A.

ACKNOWLEDGMENTS

REFERENCES

Aldheeb MA, Asrar W, Omar AA, Altaf A, Sulaeman E (2020) Effect of directionally porous wing tip on tip vortex. J Appl Fluid Mech 13(2):651-665. https://doi.org/10.29252/jafm.13.02.29738

Aldheeb MA, Asrar W, Sulaeman E, Omar AA (2016) A review on aerodynamics of non-flapping bird wings. J Aerosp Technol Manag 8(1):7-17. https://doi.org/10.5028/jatm.v8i1.564

Aldheeb MA, Asrar W, Sulaeman E, Omar AA (2018) Aerodynamics of porous airfoils and wings. Acta Mech 229(9):3915-3933. https://doi.org/10.1007/s00707-018-2203-6

Ali N, Alam M, Hossain A, Ahmed I (2017) Study on bird's & insect's wing aerodynamics and comparison of its analytical value with standard airfoil. AIP Conf Proc 185(1):020056. https://doi.org/10.1063/1.4984685

Ananda GK, Selig MS (2018) Design of bird-like airfoils. Paper presented 2018 AIAA Aerospace Sciences Meeting. AIAA; Kissimmee, Florida, USA. https://doi.org/10.2514/6.2018-0310

Béguin B, Breitsamter C (2014) Effects of membrane pre-stress on the aerodynamic characteristics of an elasto-flexible morphing wing. Aerosp Sci Technol 37:138-150. https://doi.org/10.1016/j.ast.2014.05.005

Bonnin V (2016) From albatross to long range UAV flight by dynamic soaring (thesis). Bristol: University of the West of England.

Carruthers AC, Walker SM, Thomas ALR, Taylor GK (2010) Aerodynamics of aerofoil sections measured on a free-flying bird. Proc Inst Mech Eng G J Aerosp Eng 224(8):855-864. https://doi.org/10.1243/09544100JAERO737

Chapin VG, Benard E (2015) Active control of a stalled airfoil through steady or unsteady actuation jets. J Fluids Eng 137(9):091103. https://doi.org/10.1115/1.4030483

Dvořák R (2016) Aerodynamics of bird flight. EPJ Web Conf 114:01001. https://doi.org/10.1051/epjconf/201611401001

Economon TD, Palacios F, Copeland SR, Lukaczyk TW, Alonso JJ (2016) SU2: An open-source suite for multiphysics simulation and design. AIAA J 54(3):828-845. https://doi.org/10.2514/1.J053813

Eppler R (1999) Airfoils with boundary layer suction, design and off-design cases. Aerosp Sci Technol 3(7):403-415. https://doi.org/10.1016/S1270-9638(99)00105-4

Fish FE, Weber PW, Murray MM, Howle LE (2016) The tubercles on humpback whales' flippers: Application of bio-inspired technology. Integr Comp Biol 51(1):203-213. https://doi.org/10.1093/icb/icr016

Flint TJ, Jermy MC, New TH, Ho WH (2017) Computational study of a pitching bio-inspired corrugated airfoil. Int J Heat Fluid Flow 65:328-341. https://doi.org/10.1016/j.ijheatfluidflow.2016.12.009

Ge C, Ren L, Liang P, Zhang C, Zhang Z (2013) High-lift effect of bionic slat based on owl wing. J Bionic Eng 10(4):456-463. https://doi.org/10.1016/S1672-6529(13)60243-7

Geyer T, Sarradj E, Fritzsche C (2010) Porous Airfoils: Noise reduction and boundary layer effects. Int J Aeroacoust 9(6):787-820. https://doi.org/10.1260/1475-472X.9.6.787

Iosilevskii G (2011) Aerodynamics of permeable membrane wings. Eur J Mech B/Fluids 30(5):534-542. https://doi.org/10.1016/j.euromechflu.2011.05.003

Iosilevskii G (2013) Aerodynamics of permeable membrane wings. Part 2: Seepage drag. Eur J Mech B/Fluids 39:32-41. https://doi.org/10.1016/j.euromechflu.2012.11.004

Jacob JD (1998) On the fluid dynamics of adaptive airfoils. Paper presented Proceedings of 1998 ASME International Mechanical Engineering Congress and Exposition. ASME; Anaheim, California, USA. [accessed 16 Oct 2019]

Jiao Y, Lu Y (2015) Parameter optimization research on lift-enhancing of multi-element airfoil using air-blowing. Procedia Eng 99:73-81. https://doi.org/10.1016/j.proeng.2014.12.510

Kozlov A, Chowdhury H, Mustary I, Loganathan B, Alam F (2015) Bio-inspired design: aerodynamics of boxfish. Procedia Eng 105:323-328. https://doi.org/10.1016/j.proeng.2015.05.007

Lees JJ, Dimitriadis G, Nudds RL (2016) The influence of flight style on the aerodynamic properties of avian wings as fixed lifting surfaces. PeerJ 4:e2495. https://doi.org/10.7717/peerj.2495

Malik K, Aldheeb MA, Asrar W, Sulaeman E (2019) Effects of bio-inspired surface roughness on a swept back tapered NACA 4412 wing. J Aerosp Technol Manag 11:e1719. https://doi.org/10.5028/jatm.v11.1021

Mandadzhiev BA, Lynch MK, Chamorro LP, Wissa AA (2016) Alula-inspired leading edge device for low Reynolds number flight. Paper presented Proceedings of the ASME 2016 Conference on Smart Materials, Adaptive Structures and Intelligent Systems SMASIS2016. ASME; Stowe, Vermont, USA. https://doi.org/10.1115/SMASIS2016-9210

Mandadzhiev BA, Lynch MK, Chamorro LP, Wissa AA (2017) An experimental study of an airfoil with a bio-inspired leading edge device at high angles of attack. Smart Mater Struct 26(9):094008 https://doi.org/10.1088/1361-665X/aa7dcd

Mesh Quality: ANSYS (2009) Release 12.0 © ANSYS. [accessed 25 Mar 2020]. https://www.afs.enea.it/project/neptunius/docs/fluent/html/ug/node167.htm

Müller W, Patone G (1998) Air transmissivity of feathers. J Exp Biol, 201(18):2591-2599.

NASA Turbulence modeling resource: Langley Research Center (2017) VERIF/2DANW: 2D Airfoil Near-Wake Verification Case - Intro Page. [accessed 20 Mar 2020]. https://turbmodels.larc.nasa.gov/airfoilwakeverif500c.html

NASA Turbulence modeling resource: Langley Research Center (2019) 2DN44: 2D NACA 4412 Airfoil Trailing Edge Separation [accessed 20 Mar 2020]. https://turbmodels.larc.nasa.gov/naca4412sep_val.html

NASA Turbulence modeling resource: Langley Research Center (2020) 2DN00: 2D NACA 0012 Airfoil Validation Case. [accessed 20 Mar 2020]. https://turbmodels.larc.nasa.gov/naca0012_val.html

Pennycuick CJ (1972) Soaring behaviour and performance of some east African birds, observed from a motor-glider. Ibis 114(2):178-218. https://doi.org/10.1111/j.1474-919X.1972.tb02603.x

Sachs G, Traugott J, Nesterova AP, Bonadonna F (2013) Experimental verification of dynamic soaring in albatrosses. J Exp Biol 216(22):4222-4232. https://doi.org/10.1242/jeb.085209

Selig MS, Donovan JF, Fraser DB (1989) Airfoils at low speeds. Virginia: H.A. Stokely.

Sheppard KA, Rival DE (2018) On the high-lift characteristics of a bio-inspired, slotted delta wing. Bioinspir Biomim 13(3):036008. https://doi.org/10.1088/1748-3190/aaafbd

Shyy W, Lian Y, Tang J, Viieru D, Liu H (2007) Aerodynamics of low Reynolds number flyers. Cambridge: Cambridge University Press. https://doi.org/10.1017/CBO9780511551154

Tang D, Fan Z, Lei M, Lv B, Yu L, Cui H (2019) A combined airfoil with secondary feather inspired by the golden eagle and its influences on the aerodynamics. Chin Phys B 28(3):034702. https://doi.org/10.1088/1674-1056/28/3/034702

Thielicke W (2014) The flapping flight of birds: Analysis and application (Thesis). Groningen: University of Groningen. In English.

Tobalske BW (2007) Biomechanics of bird flight. J Exp Biol 210(18):3135-3146. https://doi.org/10.1242/jeb.000273

Tucker VA, Heine C (1990) Aerodynamics of gliding flight in a Harris' Hawk, Parabuteo unicinctus. J Exp Biol 149(1):469-489.

Tucker VA, Parrott GC (1970) Aerodynamics of gliding flight in a falcon and other birds. J Exp Biol 52(2):345-367.

UIUC (2020) Airfoil Database: © 2020 UIUC Applied Aerodynamics Group. [accessed 24 Oct 2016]. https://m-selig.ae.illinois.edu/ads/coord/e193.dat

Usherwood JR (2009) The aerodynamic forces and pressure distribution of a revolving pigeon wing. Exp Fluids 46(5):991-1003. https://doi.org/10.1007/s00348-008-0596-z

Videler J, Groenewold A (1991) Field measurements of hanging flight aerodynamics in the kestrel Falco tinnunculus. J Exp Biol 155(1):519-530.

White FM (2008) Handbook fluid mechanics. Pennsylvania: McGraw-Hill Series.

Withers PC (1981) An aerodynamic analysis of bird wings as fixed aerofoils. J Exp Biol 90(1):143-162.

XFLR5 [Internet]. 2019. [accessed 22 Dec 2016]. http://www.xflr5.tech/xflr5.htm

Yang W, Song B (2017) Experimental investigation of aerodynamics of feather-covered flapping wing. Journal of Appl Bionics and Biomech 2017:3019640. https://doi.org/10.1155/2017/3019640

Yu H-T (2014) Unsteady aerodynamics of pitching flat plates wings (Thesis). Michigan: University of Michigan. In English.

Zhao G, Zhao Q (2014) Parametric analyses for synthetic jet control on separation and stall over rotor airfoil. Chinese J Aeronaut 27(5):1051-1061. https://doi.org/10.1016/j.cja.2014.03.023